Advances in Materials Research, *Vol. 12, No. 2 (2023) 133-159*
https://doi.org/10.12989/amr.2023.12.2.133

Dynamic analysis of a porous microbeam model based on refined beam strain gradient theory via differential quadrature hierarchical finite element method

Ahmed Saimi*[1,2], Ismail Bensaid[1a] and Ihab Eddine Houalef[1b]

[1]*IS2M Laboratory*, *Faculty of Technology*, *University of Tlemcen*, *Algeria*
[2]*National Higher School of Hydraulic*, *Blida*, *Algeria*

(Received April 15, 2022, Revised December 27, 2022, Accepted January 2, 2023)

Abstract. In this paper, a size-dependent dynamic investigation of a porous metal foams microbeams is presented. The novelty of this study is to use a metal foam microbeam that contain porosities based on the refined high order shear deformation beam model, with sinusoidal shear strain function, and the modified strain gradient theory (MSGT) for the first time. The Lagrange's principle combined with differential quadrature hierarchical finite element method (DQHFEM) are used to obtain the porous microbeam governing equations. The solutions are presented for the natural frequencies of the porous and homogeneous type microbeam. The obtained results are validated with the analytical methods found in the literature, in order to confirm the accuracy of the presented resolution method. The influences of the shape of porosity distribution, slenderness ratio, microbeam thickness, and porosity coefficient on the free vibration of the porous microbeams are explored in detail. The results of this paper can be used in various design for metallic foam micro-structures in engineering.

Keywords: DQHFEM; free vibration; metal foam microstructures; microbeam; modified strain gradient theory; porosity

1. Introduction

Recently, materials with a porous structure have attracted the attention of several researchers, because of their special mechanical characteristics, among these porous materials we find metal foams which have a great advantage like low masse density, good protection from temperature, good insulation of sound and a very good absorption of energy and electromagnetic waves. In the literature, one can find various researches on porous structures. Among the first works in this field, we find the works of (Wattanasakulpong *et al.* 2012), who worked on the impact of the presence of porosities in functionally graded materials realized by a process of sequential infiltration in several stages. They determined that it is important to consider the porosity effect when designing and

*Corresponding author, Ph.D., E-mail: ahmedsaimi@hotmail.fr
[a]Ph.D.
[b]Ph.D. Student

http://www.techno-press.org/?journal=amr&subpage=5 ISSN: 2234-0912 (Print), 2234-179X (Online)

studying the behaviour of FGM structures. In another study, (Wattanasakulpong and Ungbhakorn 2014) investigated the nonlinear and linear dynamic responses of FGM beams made of porous materials and taking in consideration the fixed boundary supports. (Jabbari *et al.* 2014) presented an analysis on the buckling of a circular shaped plate made of porous metallic foam material. (Chen *et al.* 2015) made a study on the elastic buckling and the static bending of porous beams made of metal foam via the theory of Timoshenko's beam. In their work (Chen *et al.* 2016), they also studied the non-linear free vibrations of a porous foam metal sandwich beam. (Rezaei and Saidi 2016) did a work on the free vibration of thick rectangular plates made of porous metal foam using the unified Carrera formulation. (Barati and Zenkour 2017) examined the post-buckling behaviour of metal foam nanobeams with imperfect geometry. (Bensaid and Guenanou 2017) investigated the static deflection and buckling of functionally graded (FG) nanoscale beams in porous material and are made based on the nonlocal Timoshenko beam model that captures small-scale influences. (Thang *et al.* 2018) investigated the stability and dynamic behaviour of porous cell plates with uniform and non-uniform porosity variations using first-order shear deformation theory. (Ebrahimi and Jafari 2018) investigated the thermomechanical performance of porous FG beams subjected to various thermal loads with two distinct porosity distributions using the improved four-variable shear-strain beam theory. Using the generalized differential quadrature approach (GDQM), (Bensaid and Saimi 2022) investigated the dynamic analysis of a viscoelastic beam made of functionally graded porous materials (FGM). With new technological advancements, extreme requirements based on the use of micro/nano electromechanical systems (MEMS/NEMS) such as actuators, thin films, sensors, probes, etc. have been raised by different industries (Stölken and Evans 1998). However, experiments indicate that the mechanical behaviour of micro/nano elements cannot be studied by classical continuum theories (CCT), due to their limitations in capturing the scaling effect. More reliable prediction can be obtained using higher order continuum theories (HOCT) in which additional hardware parameters and scales are required (Fleck *et al.* 1994). In order to study the size effect in micro and nano structures, in the literature, several have proposed non-classical theories of continuum mechanics. Among these theories is the work of (Lim *et al.* 2015) who presented a high order non-local strain-gradient and elasticity theory that take in to account high order stress gradients and the non -locality of the deformation gradient. The theory of strain gradient elasticity was introduced by the work of (Mindlin 1965), hence the density of potential energy depends on the first and second gradients of the deformation. (Lam *et al.* 2003) made an observation on the effect of the size of the structure when it is reduced to the micro/nano scale, from the experimental results, which allowed the application of the order equilibrium conditions to strain gradient elasticity theory and the number of independent elastic length scale parameters is reduced from five to three, (Lam *et al.* 2003) suggested a Modified Stress Gradient Theory (MSGT), from which a new upper-order measurements were used to characterise stress gradient behaviours. This theory proposes that the strain energy density is dependent on the symmetric strain, deviatoric stretch gradient and symmetric rotation gradient tensors, and also the dilation gradient vector. Within the framework of the modified deformation gradient theory, several researchers have studied the behaviours of vibration, buckling and bending of micro-structures, such as (Akgöz and Civalek 2013, Mirsalehi *et al.* 2017, Li *et al.* 2014, Thai *et al.* 2017. In the scientific research literature, some researchers have studied the mechanical characteristics of microbeams. For example, (Şimşek and Reddy 2013) analysed free vibration and static bending of microbeams with functional gradient material using modified torque stress theory and the theory of higher order beam. Based on theory of amended torque stress, the effect of temperature on the free vibrations and the buckling of

microbeams has been treated by (Ke *et al.* 2011). Using the theory of non-local elasticity and the theory of Timoshenko's beam, (Wang *et al.* 2008) have investigated the bending of isotropic microbeams. And (Wang *et al.* 2018) analysed a porous microbeam model for vibration analysis based on modified stress gradient theory and sinusoidal beam theory, via the method Analytics from Navier's. Most of the above works have used analytical or experimental methods in their studies. And also, some have used numerical methods such as the generalized differential quadrature method (Bensaid and Saimi 2022). There is also the work of (Karamanli and Aydogdu 2020) who investigate free vibration analysis of functionally graded porous microplates with shear and normal deformation via the classical finite element method. Recently a new combination between the hierarchical finite element method and the generalized differential quadrature method was applied for the study of the dynamic response of an onboard rotor (Ahmed *et al.* 2020), this method was used for the first time in the work of (Liu *et al.* 2017) for the applications to vibrations and bending of Mindlin plates with curvilinear domains. (Abdelrahman *et al.* 2021) presented a dynamic finite elements procedure capable of analysing the dynamic behaviour of perforated Timoshenko microbeams in thermal environment and subjected to moving mass for the first time. (Ebrahimi *et al.* 2017) investigated Thermo-mechanical vibration characteristics of in homogeneous porous functionally graded (FG) micro/nanobeam subjected to various types of thermal loadings based on modified couple stress theory with consideration of the exact position of neutral axis. For the first time, (Chai and Wang 2022) explores the traveling wave vibration characteristics of spinning graphene platelets reinforced metal foam (GPLRMF) connected conical-cylindrical shells (JCCSs). (Wang *et al.* 2019) employs an updated Donnell nonlinear shell theory to analyse the nonlinear vibrations of metal foam circular cylindrical shells supplemented with graphene platelets. (Ye and Wang 2021) investigated the nonlinear forced vibration of thin-walled metal foam cylindrical shells reinforced with functionally graded graphene platelets, hence, three kinds of porosity distribution and different kinds of graphene platelet distribution are considered. (Teng and Wang 2021) studied nonlinear forced vibration of graphene platelet reinforced porous metal foam (GPLRMF) rectangular plates. A spinning functionally graded graphene platelet-reinforced metal foam (FG-GPLRMF) beam's free vibration is investigated by (Xu *et al.* 2021). For the first time, the differential transformation approach is extended to study flap-wise bending vibration and chord-wise bending vibration with Coriolis force effect. In the work done by (Wang and Zu 2017) the vibrations of functionally graded material (FGM) rectangular plates with porosities moving in a thermal environment are studied for the first time. Because of technical issues during the production of FGMs, the FGM plates have porosities. Electro-mechanical vibrations of functionally graded piezoelectric material (FGPM) plates carrying porosities in the translation state are explored in work done by (Wang 2018) as a reference for aeronautical structural design. (Jalaei *et al.* 2022) explored the transient response of porosity-dependent viscoelastic functionally graded nanobeams and subjected to the dynamic loads and external magnetic fields. (Karamanli *et al.* 2022) analysed the size-dependent performance of metal foam microbeams considering three distinct porosity distribution models. (Karamanli *et al.* 2021) researched by a thorough investigation by finite element method the bending, vibration, and buckling behaviours of multi-directional FG microplates. The material characteristics change in both the in-plane and through-thickness directions. Based on the modified strain gradient theory and a quasi-3D shear and normal deformation plate theory. (Nguyen *et al.* 2022) proposed a basic two-variable shear deformation theory for functionally graded porous (FGP) beam bucking, bending, and vibration behaviour. The displacement field of beams is created by separating variables. A finite element model for the structural behaviours of

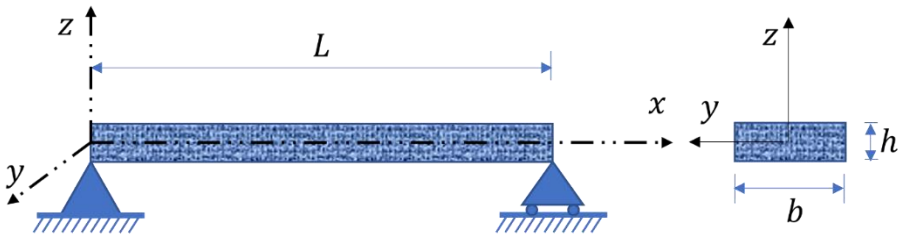

Fig. 1 Porous microbeam with simple supports and its straight section

bi-directional (2D) FG porous microbeams is proposed in (Karamanli and Vo 2021a), which is based on a quasi-3D theory and the modified strain gradient theory (MSGT). A generalized nonlocal beam theory is developed in the paper (Aydogdu 2009) to analyse the bending, buckling, and free vibration of nanobeams. The size-dependent responses of functionally graded (FG) porous microbeams are explored in (Karamanli and Vo 2021b) utilizing a quasi-3D theory and the modified strain gradient theory. The eigenfrequencies of rotating laminated composite (LC) and sandwich microbeams with various boundary conditions (BCs) are investigated in (Karamanli and Aydogdu 2019).

To the authors' knowledge, and by searching in the literature, we found that no study has been conducted on the free vibration analysis of the porous metal foam microbeams by combining the differential quadrature hierarchical finite elements method (DQHFEM) and the refined high order shear deformation beam theory, considering the sinusoidal type shear deformation function, in conjunction with the modified strain gradient theory, which takes into account the scale effect. In this context, the present article tries to give a robust numerical investigation on this case and studying this topic comprehensively. Three models of porosity distribution namely uniform (UDP), symmetric (NUDP1) and asymmetric (NUDP2) distributions are considered. This study incorporates three material length scale parameters that can capture the size effect of porous microbeams with high accuracy. Then, the obtained solutions by the current method are validated with existing analytical methods in the literature. Subsequently, the impact of many important parameters on the free vibration of porous metal foam microbeams are explored.

2. Formulation and theories

2.1 Model of porous microbeam

In this work, we consider a micro-beam of porous metal foam, with the following geometric properties: a length L, a width b, and a thickness h, as shown in Fig. 1.

The distribution of porosity in the microbeam is assumed through the direction of the thickness, according to three models of distribution of porosity such as: (a) the uniform distribution of porosity (UDP), (b) the non-uniform distribution of porosity 1 (NUDP1) which is symmetrical, and (c) the non-uniform distribution of porosity 2 (NUDP2) which is asymmetrical, as shown in Fig. 2.

The properties of the material, such as the Young E module and the density ρ, change according to the type of porosity distribution. For UDP, the young's module E and the masse density ρ have constants value according to the thickness of the micro beam direction, as shown in Fig. 2.

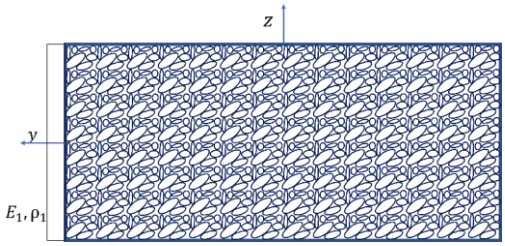

Fig. 2 Uniform distribution of porosity in thickness direction (UDP)

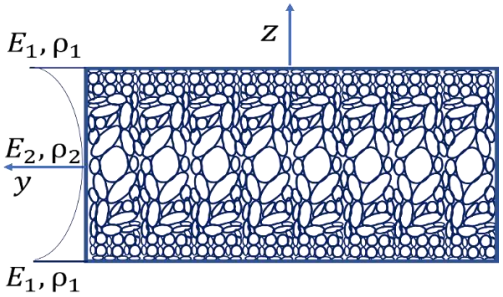

Fig. 3 Non-uniform distribution of porosity 1 in thickness direction (NUDP1)

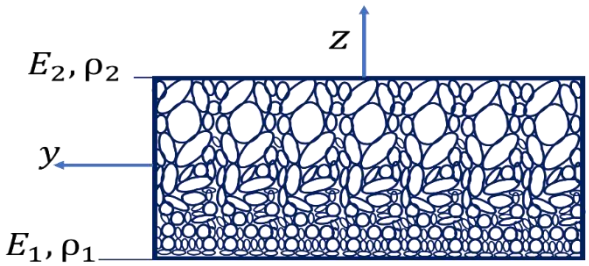

Fig. 4 Non-uniform distribution of porosity 2 in thickness direction (NUDP2)

However, for case of NUDP1, the young's module E and the masse density ρ, have maximum values in the extreme high and extreme low surfaces, and the smallest values are in the middle axis of the micro beam, see Fig. 3. For the case NUDP2, the young's module E and the masse density ρ, have maximum values in the low extreme surface area, and minimum values in the high extreme surface area of the micro beam. See Fig. 4.

The distribution of the material properties of the porous microbeam, takes the form according to the following equations (Chen *et al.* 2016, Chen *et al.* 2015)

$$UDP: \begin{cases} E = E_1(1 - e_0\zeta) \\ \rho = \rho_1\sqrt{(1 - e_0\zeta)} \end{cases} \tag{1}$$

$$NUDP1: \begin{cases} E(z) = E_1\left(1 - e_0\cos\left(\frac{\pi z}{h}\right)\right) \\ \rho(z) = \rho_1\sqrt{\left(1 - e_m\cos\left(\frac{\pi z}{h}\right)\right)} \end{cases} \tag{2}$$

$$NUDP2: \begin{cases} E(z) = E_1\left(1 - e_0 \cos\left(\frac{\pi z}{2h} + \frac{\pi}{4}\right)\right) \\ \rho(z) = \rho_1\sqrt{\left(1 - e_m \cos\left(\frac{\pi z}{2h} + \frac{\pi}{4}\right)\right)} \end{cases} \tag{3}$$

With

$$\begin{cases} e_0 = 1 - \frac{E_2}{E_1} \\ e_m = 1 - \frac{\rho_2}{\rho_1} \\ \zeta = \frac{1}{e_0} - \frac{1}{e_0}\left(\frac{2}{\pi}\sqrt{1 - e_0} - \frac{2}{\pi} + 1\right)^2 \end{cases} \tag{4}$$

Hence, ρ_1 and E_1 are minimum values of masse density and young's module respectively. E_2 and ρ_2 are maximum young module values and density respectively. e_0 and e_m are the porosity and mass porosity coefficients respectively.

e_0 is the primary variable used to characterize porosity, and e_m is determined by their relationship, which is obtained from the normal mechanical properties of an open-cell metal foam. Due to the increasing size and density of interior pores, a larger value of e_0 corresponds to lower elastic modulus and mass density. It should be noticed that $e_0 = e_m = 0$ denotes a particular circumstance in which no pore occurs in the core, but $e_0 = e_m = 1$ is not possible because all material property values are lowered to zero in this instance. The porosity coefficient value is limited between $0 \leq e_0 < 1$.

2.2 Strain gradient elasticity theory

According to the Modified Couple Strain Theory (MCST) of (Yang *et al.* 2002), in addition to the rotationally symmetrical gradient tensor, (Lam *et al.* 2003) incorporated an extra dilatation gradient tensor and the tensor of deviatoric stretch gradient, resulting in the Modified Strain Gradient Theory of Elasticity (MSGT). These tensors are separated by two standard material constants for isotropic linear elastic materials and three different material length scale parameters. The formula for strain energy, according to these theories, is as follows

$$U = \frac{1}{2}\int_0^L \int_A \left(\sigma_{ij}\varepsilon_{ij} + p_i\gamma_i + \tau_{ijk}^{(1)}\eta_{ijk}^{(1)} + m_{ij}^s\chi_{ij}^s\right) dAdx \tag{5}$$

Hence $\varepsilon_{ij}, \gamma_i, \eta_{ijk}^{(1)}$, and χ_{ij}^s represents respectively the strain tensor, the deviatoric stretching gradient tensor, the dilatation gradient tensor, and the rotationally symmetric gradient tensor which are defined by the following equations, a subscripted comma is used to denote the derivative with respect to the followed variable.

$$\varepsilon_{ij} = \frac{1}{2}\left(u_{i,j} + u_{j,i}\right) \tag{6}$$

$$\gamma_i = \varepsilon_{mm,i} \tag{7}$$

$$\eta_{ijk}^{(1)} = \frac{1}{3}\left(\varepsilon_{jk,i} + \varepsilon_{ki,j} + \varepsilon_{ij,k}\right) - \frac{1}{15}\left[\delta_{ij}\left(\varepsilon_{mm,k} + 2\varepsilon_{mk,m}\right) + \delta_{jk}\left(\varepsilon_{mm,i} + 2\varepsilon_{mi,m}\right) + \delta_{ki}\left(\varepsilon_{mm,j} + 2\varepsilon_{mj,m}\right)\right] \tag{8}$$

$$\chi_{ij}^{s} = \frac{1}{2}\left(\theta_{i,j} + \theta_{j,i}\right) \tag{9}$$

$$\theta_i = \frac{1}{2} e_{ijk} u_{k,j} \tag{10}$$

Where u_i, θ_i, δ_{ij} and e_{ijk} are the components of displacement vector, the components of rotation vectors, the Kronecker delta and the permutation symbols, respectively.

$$\sigma_{ij} = \lambda \varepsilon_{mm} \delta_{ij} + 2\mu \varepsilon_{ij} \tag{11}$$

$$p_i = 2\mu l_0^2 \gamma_i \tag{12}$$

$$\tau_{ijk}^{(1)} = 2\mu l_1^2 \eta_{ijk}^{(1)} \tag{13}$$

$$m_{ij}^{s} = 2\mu l_2^2 \chi_{ij}^{s} \tag{14}$$

σ is the classical stress tensor. p, $\tau^{(1)}$ and m^s are the higher order strain tensors.

The independent parameters of the dilatation, deviatory stretching, and symmetrical rotational gradients-related material length scale, respectively, are represented by l_0, l_1 and l_2.

$$\mu = \frac{E}{2(1+\nu)} \tag{15}$$

$$\lambda = \frac{E\nu}{(1+\nu)(1-2\nu)} \tag{16}$$

Hence μ and λ are the Lame constants, and ν is the Poisson's ratio.

2.3 Kinematics formulation

Based on a refined beam strain gradient theory, the displacement field at any arbitrary location on the microbeam is assumed to be stated as follows in the current work (Thai and Vo 2012)

$$\begin{cases} u_1(x,z,t) = u_0(x,t) - z\dfrac{dw_b}{dx} + f(z)\dfrac{dw_s}{dx} \\ u_2(x,z,t) = 0 \\ u_3(x,z,t) = w_b(x,t) + w_s(x,t) \end{cases} \tag{17}$$

According to this theory, the transverse displacement is divided into two parts bending w_b and shear w_s.

Where u_0, w_b and w_s are respectively, the displacement in the plane in the directions $x -$, the bending and shear components of the transverse displacement of the points on the neutral axis of the beam.

In this work, our choice of functions is determined on the basis of the given sinusoidal shear function (Touratier 1991)

$$f(z) = \left(\frac{h}{\pi}\right) * \sin\left(\pi \frac{z}{h}\right) \tag{18}$$

By introducing Eqs. (17) and (18) into Eq. (6), we obtain the non-zero deformation torsor components

$$\begin{cases} \varepsilon_{11} = \frac{du}{dx} - z\frac{d^2w_b}{dx^2} + f\frac{d^2w_s}{dx^2} \\ \varepsilon_{13} = \frac{1}{2}\left(\left(\frac{df}{dz}+1\right)\frac{dw_s}{dx}\right) \end{cases} \tag{19}$$

By replacing Eq. (19) in (11) we obtain the strain tensor

$$\begin{cases} \sigma_{11} = \left(\frac{E(1-\nu)}{(1-2\nu)(1+\nu)}\right)\varepsilon_{11} = \left(\frac{\lambda}{\nu}-\lambda\right)\varepsilon_{11} \\ \sigma_{22} = \sigma_{33} = \frac{E\nu}{(1-2\nu)(1+\nu)}\varepsilon_{11} = \lambda\varepsilon_{11} \\ \sigma_{13} = \frac{E}{(1+\nu)}\varepsilon_{xz} = 2\mu\varepsilon_{13} \end{cases} \tag{20}$$

Based on Eqs. (19) and (7), the non-zeros components of the dilatation gradient vector are inscribed as follows

$$\begin{cases} \gamma_1 = \frac{d^2u}{dx^2} - z\frac{d^3w_b}{dx^3} + f\frac{d^3w_s}{dx^3} \\ \gamma_3 = -\frac{d^2w_b}{dx^2} + \frac{df}{dz}\frac{d^2w_s}{dx^2} \end{cases} \tag{21}$$

By replacing Eqs. (21) in (12) we obtain the non-zero higher order constraints p_i are expressed by

$$\begin{cases} p_1 = 2\mu {l_0}^2\left(\frac{d^2u}{dx^2} - z\frac{d^3w_b}{dx^3} + f\frac{d^3w_s}{dx^3}\right) \\ p_3 = -2\mu {l_0}^2\left(\frac{d^2w_b}{dx^2} - \frac{df}{dz}\frac{d^2w_s}{dx^2}\right) \end{cases} \tag{22}$$

Applying Eq. (19) in (8), we will have the components non-zero of the deviatoric stretching gradient tensor $\eta^{(1)}$, such as

$$\begin{cases} \eta_{111} = \frac{1}{5}\left[2\left(\frac{d^2u}{dx^2} - z\frac{d^3w_b}{dx^3} + f\frac{d^3w_s}{dx^3}\right) - \left(\frac{df}{dz}+1\right)\frac{d^2w_s}{dx^2}\right] \\ \eta_{113} = \eta_{131} = \eta_{113} = -\frac{4}{15}\left[\frac{d^2w_b}{dx^2} - \frac{df}{dz}\frac{d^2w_s}{dx^2} - \frac{d^2f}{dz^2}\frac{dw_s}{dx}\right] \\ \eta_{122} = \eta_{212} = \eta_{221} = -\frac{1}{15}\left[3\left(\frac{d^2u}{dx^2} - z\frac{d^3w_b}{dx^3} + f\frac{d^3w_s}{dx^3}\right) + \frac{d^2f}{dz^2}\frac{dw_s}{dx}\right] \\ \eta_{133} = \eta_{313} = \eta_{331} = -\frac{4}{15}\left[\frac{3}{4}\left(\frac{d^2u}{dx^2} - z\frac{d^3w_b}{dx^3} + f\frac{d^3w_s}{dx^3}\right) - \frac{d^2f}{dz^2}\frac{dw_s}{dx}\right] \\ \eta_{223} = \eta_{232} = \eta_{322} = \frac{1}{15}\left[\frac{d^2w_b}{dx^2} - \left(2\frac{df}{dz}+1\right)\frac{d^2w_s}{dx^2}\right] \\ \eta_{333} = \frac{1}{5}\left[\frac{d^2w_b}{dx^2} - \left(2\frac{df}{dz}+1\right)\frac{d^2w_s}{dx^2}\right] \end{cases} \tag{23}$$

The substitution of Eq. (23) in Eq. (13), leads to give the non-zero higher order constraints $\tau^{(1)}$

$$\begin{cases} \tau^{(1)}_{111} = \frac{2}{5}\mu {l_1}^2\left[2\left(\frac{d^2u}{dx^2} - z\frac{d^3w_b}{dx^3} + f\frac{d^3w_s}{dx^3}\right) - \left(\frac{df}{dz}+1\right)\frac{d^2w_s}{dx^2}\right] \\ \tau^{(1)}_{113} = \tau^{(1)}_{131} = \tau^{(1)}_{311} = -\frac{8}{15}\mu {l_1}^2\left[\frac{d^2w_b}{dx^2} - \frac{df}{dz}\frac{d^2w_s}{dx^2} - \frac{d^2f}{dz^2}\frac{dw_s}{dx}\right] \\ \tau^{(1)}_{122} = \tau^{(1)}_{212} = \tau^{(1)}_{221} = -\frac{2}{15}\mu {l_1}^2\left[3\left(\frac{d^2u}{dx^2} - z\frac{d^3w_b}{dx^3} + f\frac{d^3w_s}{dx^3}\right) + \frac{d^2f}{dz^2}\frac{dw_s}{dx}\right] \\ \tau^{(1)}_{133} = \tau^{(1)}_{313} = \tau^{(1)}_{331} = -\frac{8}{15}\mu {l_1}^2\left[\frac{3}{4}\left(\frac{d^2u}{dx^2} - z\frac{d^3w_b}{dx^3} + f\frac{d^3w_s}{dx^3}\right) - \frac{d^2f}{dz^2}\frac{dw_s}{dx}\right] \\ \tau^{(1)}_{223} = \tau^{(1)}_{232} = \tau^{(1)}_{322} = \frac{2}{15}\mu {l_1}^2\left[\frac{d^2w_b}{dx^2} - \left(2\frac{df}{dz}+1\right)\frac{d^2w_s}{dx^2}\right] \\ \tau^{(1)}_{333} = \frac{2}{5}\mu {l_1}^2\left[\frac{d^2w_b}{dx^2} - \left(2\frac{df}{dz}+1\right)\frac{d^2w_s}{dx^2}\right] \end{cases} \tag{24}$$

Introducing Eq. (17) into (10) gives

$$\begin{cases} \theta_1 = 0 \\ \theta_2 = -\left(\frac{dw_b}{dx} - \frac{1}{2}\left(\frac{df}{dz} - 1\right)\frac{dw_s}{dx}\right) \\ \theta_3 = 0 \end{cases} \tag{25}$$

The non-zero components of rotationally symmetrical gradient tensor χ^s are obtained by replacing Eq. (25) in Eq. (9)

$$\begin{cases} \chi_{23}^s = \chi_{32}^s = \frac{1}{4}\left(\frac{d^2 f}{dz^2}\right)\frac{dw_s}{dx} \\ \chi_{12}^s = \chi_{21}^s = -\frac{1}{2}\left(\frac{d^2 w_b}{dx^2} - \frac{1}{2}\left(\frac{df}{dz} - 1\right)\frac{d^2 w_s}{dx^2}\right) \end{cases} \tag{26}$$

Replacing Eq. (26) in Eq. (14) gives the non-zero higher order constraints m_{ij}^s such as

$$\begin{cases} m_{23}^s = m_{32}^s = \frac{\mu {l_2}^2}{2}\left(\frac{d^2 f}{dz^2}\right)\frac{dw_s}{dx} \\ m_{12}^s = m_{21}^s = -\mu {l_2}^2\left(\frac{d^2 w_b}{dx^2} - \frac{1}{2}\left(\frac{df}{dz} - 1\right)\frac{d^2 w_s}{dx^2}\right) \end{cases} \tag{27}$$

The substitution of Eqs. (19)-(27) in Eq. (5)

$$U = {U_e}^1 + {U_e}^2 + {U_e}^3 + {U_e}^4 \tag{28}$$

Such as

$${U_e}^1 = \frac{1}{2}\int_0^l \left[I_1\left(\frac{du}{dx}\right)^2 - 2I_2\frac{du}{dx}\frac{d^2 w_b}{dx^2} + 2I_3\frac{du}{dx}\frac{d^2 w_s}{dx^2} - 2I_4\frac{d^2 w_b}{dx^2}\frac{d^2 w_s}{dx^2} + I_5\left(\frac{d^2 w_b}{dx^2}\right)^2 + I_6\left(\frac{d^2 w_s}{dx^2}\right)^2 + I_7\left(\frac{dw_s}{dx}\right)^2\right]dx \tag{29}$$

$${U_e}^2 = \frac{1}{2}\int_0^l \left(B_1\left(\left(\frac{d^2 u}{dx^2}\right)^2 + \left(\frac{d^2 w_b}{dx^2}\right)^2\right) - 2B_2\frac{d^2 u}{dx^2}\frac{d^3 w_b}{dx^3} + 2B_3\frac{d^2 u}{dx^2}\frac{d^3 w_s}{dx^3} - 2B_4\frac{d^3 w_b}{dx^3}\frac{d^3 w_s}{dx^3} + B_5\left(\frac{d^3 w_b}{dx^3}\right)^2 + B_6\left(\frac{d^3 w_s}{dx^3}\right)^2 - 2B_7\frac{d^2 w_b}{dx^2}\frac{d^2 w_s}{dx^2} + B_8\left(\frac{d^2 w_s}{dx^2}\right)^2\right)dx \tag{30}$$

$${U_e}^3 = \frac{1}{2}\int_0^l \left[R_1\left(\left(\frac{d^2 u}{dx^2}\right)^2 + \frac{2}{3}\left(\frac{d^2 w_b}{dx^2}\right)^2\right) - 2R_2\frac{d^2 u}{dx^2}\frac{d^3 w_b}{dx^3} + 2R_3\frac{d^2 u}{dx^2}\frac{d^3 w_s}{dx^3} - 2R_4\frac{d^3 w_b}{dx^3}\frac{d^3 w_s}{dx^3} + R_5\left(\frac{d^3 w_b}{dx^3}\right)^2 + R_6\left(\frac{d^3 w_s}{dx^3}\right)^2 + \frac{2}{3}R_7\left(\frac{dw_s}{dx}\right)^2 - R_8\frac{d^2 u}{dx^2}\frac{dw_s}{dx} + R_9\frac{d^3 w_b}{dx^3}\frac{dw_s}{dx} - R_{10}\frac{d^3 w_s}{dx^3}\frac{dw_s}{dx} - \frac{4}{3}R_{11}\frac{d^2 w_b}{dx^2}\frac{d^2 w_s}{dx^2} + \frac{2}{3}R_{12}\left(\frac{d^2 w_s}{dx^2}\right)^2\right]dx \tag{31}$$

$${U_e}^4 = \frac{1}{2}\int_0^l \left(D_1\left(\frac{d^2 w_b}{dx^2}\right)^2 + \frac{1}{4}D_2\left(\frac{dw_s}{dx}\right)^2 - D_3\frac{d^2 w_b}{dx^2}\frac{d^2 w_s}{dx^2} + \frac{1}{4}D_4\left(\frac{d^2 w_s}{dx^2}\right)^2\right)dx \tag{32}$$

With

$$\{I_1, I_2, I_3, I_4, I_5, I_6\} = b\int_{-\frac{h}{2}}^{\frac{h}{2}}\left(\frac{\lambda}{\nu} - \lambda\right)(1, z, f, zf, z^2, f^2)dz \quad , \{I_7\} = b\int_{-\frac{h}{2}}^{\frac{h}{2}}\mu\left(\frac{df}{dz} + 1\right)^2 dz \tag{33}$$

$$\{B_1, B_2, B_3, B_4, B_5, B_6, B_7, B_8\} = b\int_{-\frac{h}{2}}^{\frac{h}{2}} 2\mu {l_0}^2 \left(1, z, f, zf, z^2, f^2, \frac{df}{dz}, \left(\frac{df}{dz}\right)^2\right) dz \tag{34}$$

$$\{R_{1:12}\} = b\int_{-\frac{h}{2}}^{\frac{h}{2}} \frac{4}{5}\mu {l_1}^2 \left(1, z, f, zf, z^2, f^2, \left(\frac{d^2f}{dz^2}\right)^2, \frac{d^2f}{dz^2}, z\frac{d^2f}{dz^2}, f\frac{d^2f}{dz^2}, \left(2\frac{df}{dz}+1\right), \left(2\frac{df}{dz}+1\right)^2\right) dz \tag{35}$$

$$\{D_1, D_2, D_3, D_4\} = b\int_{-\frac{h}{2}}^{\frac{h}{2}} \mu {l_2}^2 \left(1, \left(\frac{d^2f}{dz^2}\right)^2, \left(\frac{df}{dz}-1\right), \left(\frac{df}{dz}-1\right)^2\right) dz \tag{36}$$

The Kinetic Energy can be written as

$$T = \frac{1}{2}\int_0^l \int_A \left[{\dot{u}_1}^2 + {\dot{u}_2}^2 + {\dot{u}_3}^2\right] dA dx \tag{37}$$

By replacing Eq. (17) in Eq. (37) we obtain the final form of the kinetic energy

$$T = \frac{1}{2}\int_0^l \left[J_1\left(\dot{u}^2 + {\dot{w}_b}^2 + {\dot{w}_s}^2 + 2\dot{w}_b\dot{w}_s\right) - 2J_2\dot{u}\frac{d\dot{w}_b}{dx} + 2J_3\dot{u}\frac{d\dot{w}_s}{dx} - 2J_4\frac{d\dot{w}_b}{dx}\frac{d\dot{w}_s}{dx} + J_5\left(\frac{d\dot{w}_b}{dx}\right)^2 + J_6\left(\frac{d\dot{w}_s}{dx}\right)^2\right] dx \tag{38}$$

Hence the mass moments of inertia

$$\{J_1, J_2, J_3, J_4, J_5, J_6\} = b\int_{-\frac{h}{2}}^{\frac{h}{2}} \rho(1, z, f, zf, z^2, f^2) dz \tag{39}$$

2.4 Differential quadrature hierarchical finite element formulation

The derivative of a function at a point is approximated by a weighted linear sum of field variables along a line through the spot using established DQ criteria. Any other complete basis, in addition to Lagrange functions, can be utilized to formulate DQ rules. ((Liu *et al.* 2017, Xing and Liu 2009, Bensaid *et al.* 2022, Ihab Eddine *et al.* 2023).

As a result, the order n derivative of a field variable $g(x)$ at a discrete location x_i can be represented as

$$\left.\frac{\partial^n g(x,t)}{\partial x^n}\right|_{x_i} = \sum_{j=1}^{N} A_{ij}^{(n)} g(x_j, t) \quad (i = 1,2,3, \ldots\ldots, N) \tag{40}$$

With $A_{ij}^{(n)}$ is the weighting coefficient related to the derivative of order n, and the weighting coefficient is obtained by the following.

If $n = 1$, then

$$\begin{aligned} A_{ij}^{(1)} &= \frac{M(x_i)}{(x_i - x_j)M(x_j)} \qquad i \neq j, i, j = 1,2, \ldots, N \\ A_{ii}^{(1)} &= -\sum_{j=1, j\neq i}^{n} A_{ij}^{(1)} \qquad i = 1,2, \ldots, N \end{aligned} \tag{41}$$

With

$$M(x_i) = \prod_{k=1,k\neq i}^{N}(x_i - x_k)$$
$$M(x_j) = \prod_{k=1,k\neq i}^{N}(x_j - x_k) \tag{42}$$

If $n > 1$, the second and higher order derivatives, the weighting coefficients are determined using the following simple recurrence relation

$$A_{ij}^{(n)} = n\left(A_{ij}^{(1)} * A_{ii}^{(n-1)} - \frac{A_{ij}^{(n-1)}}{(x_i - x_j)}\right) \quad i \neq j, i, j = 1,2,\dots,N, n > 1$$
$$A_{ii}^{(n)} = -\sum_{j=1,j\neq i}^{N} A_{ij}^{(n)} \qquad i = 1,2,\dots,N \tag{43}$$

The Gauss-Lobatto quadrature rules theory can be found in the mathematical literature; The Gauss-Lobatto quadrature rule with a degree of accuracy. $(2n-3)$ for the function $g(x)$ defined in [-1, 1] is

$$\int_{-1}^{1} f(x)dx = \sum_{j=1}^{N} C_j g(x_j) \tag{44}$$

With the weighting coefficient C_j of the Gauss-Lobatto integration is given by

$$C_1 = C_N = \frac{2}{N(N-1)}, \quad C_j = \frac{2}{N(N-1)[P_{N-1}(x_j)]^2} \quad (j \neq 1, N) \tag{45}$$

x_j is the $(j-1)$ zero of the first order derivative of $P_{N-1}(x)$. We will utilize the recursion formula as Eqs. (46) and (47) to solve the roots of Legendre polynomials; it is simple to find thousands of roots this way.

$$P_{N+1}(x) = \frac{2N+1}{N+1} x P_N(x) - \frac{N}{N+1} P_{N-1}(x) \tag{46}$$

With $P_0(x) = 1$, $P_1(x) = x$. The n-order derivation of Legendre polynomials can be determined by the following equation

$$P_{N+1}^{(n)}(x) = x P_N^{(n)}(x) + (N+n) P_N^{(n)}(x) \tag{47}$$

In order to obtain a denser population near the boundaries, the sample points are selected according to the Gauss-Lobatto grid distribution of nodes.

$$x_j = -\cos\left(\frac{j-1}{N-1}\pi\right) \tag{48}$$

The Gauss-Lobatto nodes are solved with the Newton-Raphson iteration method

$$x^{iT+1} = x^{iT} - \boldsymbol{F}'\left(x^{iT}\right)^{-1}\boldsymbol{F}\left(x^{iT}\right), \qquad iT = 0,1,\dots\dots \tag{49}$$

Were

$$x = [x_2, x_3, \dots\dots\dots, x_{N-1}]^T \tag{50}$$

$$\boldsymbol{F}(x) = [f(x_2), f(x_3), \dots, f(x_{N-1})]^T \tag{51}$$

$$\boldsymbol{F}'(x) = \left[\frac{\partial f(x_j)}{\partial x_i}\right]_{(N-2)\times(N-2)} \tag{52}$$

$$f(x_j) = \sum_{k-1,k\neq j}^{N} \frac{1}{x_j - x_k} \quad j = 2,3,\dots,N-1 \tag{53}$$

$$\frac{\partial f(x_j)}{\partial x_i} = \begin{cases} -\sum_{k=1,k\neq j}^{N} \frac{1}{(x_j - x_k)^2}, & (i = j) \\ \frac{1}{(x_j - x_i)^2}, & (i \neq j) \end{cases} \tag{54}$$

The value of x at the iT^{th} iteration step is denoted by k. This approach is less affected by the starting value. As beginning values, the values given by Eq. (48) are employed.

In this section we aim to illustrate the use of DQHFEM through the microbeam, although work has already been done for a Euler-Bernoulli uniform beam (Liu *et al.* 2017), we will follow the same steps to determine the differential equation of motion of the porous microbeam.

The displacement field used for the DQHFEM (Ahmed *et al.* 2020)

$$u[x(\xi)] = H_1(\xi)u_1 + \frac{L_e}{2}H_2(\xi)\frac{du_1}{dx} + H_3(\xi)u_2 + \frac{L_e}{2}H_4(\xi)\frac{du_2}{dx} + \sum_{n=1}^{M}\psi_n(\xi)U_n \tag{55}$$

$$w[x(\xi)] = H_1(\xi)w_1 + \frac{L_e}{2}H_2(\xi)\frac{dw_1}{dx} + H_3(\xi)w_2 + \frac{L_e}{2}H_4(\xi)\frac{dw_2}{dx} + \sum_{n=1}^{M}\psi_n(\xi)W_n \tag{56}$$

The first four functions $H_1(\xi)$, $H_2(\xi)$, $H_3(\xi)$ and $H_4(\xi)$ are those of the finite element method needed to describe the displacements and rotations at the nodes of the element, for which we use the cubic Hermite shape functions (Bardell 1996).

$$\begin{aligned} H_1(\xi) &= \tfrac{1}{4}(1-\xi)^2(2+\xi) \quad H_2(\xi) = \tfrac{1}{4}(1-\xi)^2(\xi+1) \\ H_3(\xi) &= \tfrac{1}{4}(1+\xi)^2(2-\xi) \quad H_4(\xi) = \tfrac{1}{4}(1+\xi)^2(\xi-1) \end{aligned} \tag{57}$$

Or the local coordinates are related to the dimensionless coordinates by the relation

$$x = \frac{L_e}{2}(\xi + 1) \;\; avec - 1 \leq \xi \leq 1 \tag{58}$$

And $\psi_n(\xi)$ are the hierarchical functions that contribute to the internal displacement field

$$\psi_n(\xi) = \frac{(\xi^2-1)^2}{n(n+1)(n+2)(n+3)}\frac{d^2P_{n+1}}{d\xi^2} \tag{59}$$

The low-order Legendre polynomial can be calculated from the Rodrigues form of special Legendre polynomials (Peano 1976); the generating function is listed below.

$$\begin{gathered} P_n(\xi) = \sum_{k=0}^{\frac{(n-1)}{2}} \frac{(-1)^k(2n-2k-7)!!}{2^k k!(n-2k-1)!}\xi^{(n-2k-1)} \\ with \;\; , n > 4 \\ \text{Hence } n!! = n(n-2)(n-4)\ldots(2 \; or \; 1),\; 0!! = (-1)!! = 1, \\ \text{And } (n-1)/2 \quad \text{Designates its own integer part} \end{gathered} \tag{60}$$

This Legendre polynomial expression has been used in several papers (Saimi and Hadjoui 2016, Assem *et al.* 2022, Saimi *et al.* 2021) in the *h*, *p* and *hp* versions of the finite element method.

One can also use the recursion formula in Eqs. (46)-(47), the order n can reach several thousand.

The displacement vectors of the element are noted as follows

$$\begin{aligned} \boldsymbol{u^T} &= [u_1 \;\; u'_1 \;\; u_2 \;\; u'_2 \;\; U_1 \;\; \ldots \;\; U_M] \\ \boldsymbol{w^T} &= [w_1 \;\; w'_1 \;\; w_2 \;\; w'_2 \;\; W_1 \;\; \ldots \;\; W_M] \end{aligned} \tag{61}$$

So, the equations of $u[x(\xi)]$ became

$$\begin{aligned} u[x(\xi)] &= [N_u]^T \boldsymbol{u} \\ w[x(\xi)] &= [N_w]^T \boldsymbol{w} \end{aligned} \tag{62}$$

Therefore

$$\begin{aligned} [\mathrm{N}_u]^T &= \left[H_1(\xi) \;\; -\tfrac{L_e}{2}H_2(\xi) \;\; H_3(\xi) \;\; -\tfrac{L_e}{2}H_4(\xi) \;\; \psi_1(\xi) \;\; \psi_2(\xi) \;\; \ldots \;\; \psi_M(\xi)\right] \\ [\mathrm{N}_w]^T &= \left[H_1(\xi) \;\; \tfrac{L_e}{2}H_2(\xi) \;\; H_3(\xi) \;\; \tfrac{L_e}{2}H_4(\xi) \;\; \psi_1(\xi) \;\; \psi_2(\xi) \;\; \ldots \;\; \psi_M(\xi)\right] \end{aligned} \tag{63}$$

The Gauss-Lobatto node calculation ξ_j, $j = 1,2,\ldots\ldots,N$, with $N = M + 4$. Defines the following displacement vectors

$$\begin{aligned} \bar{\boldsymbol{u}}^{\boldsymbol{T}} &= [u(x_1) \;\; u(x_2) \;\; \ldots\ldots \; u(x_N)] \\ \bar{\boldsymbol{w}}^{\boldsymbol{T}} &= [w(x_1) \;\; w(x_2) \;\; \ldots\ldots \; w(x_N)] \end{aligned} \tag{64}$$

According to Eq. (64) the relationship between (63) and (66) is defined by the following equation

$$\begin{aligned} \bar{\boldsymbol{u}} &= \boldsymbol{G_u}\, \boldsymbol{u} \\ \bar{\boldsymbol{w}} &= \boldsymbol{G_w}\, \boldsymbol{w} \end{aligned} \tag{65}$$

Were

$$\begin{aligned} \boldsymbol{G_u} &= \left[[\mathrm{N}_u](\xi_1) \quad [\mathrm{N}_u](\xi_2) \quad \ldots\ldots \quad [\mathrm{N}_u](\xi_N)\right]^{\boldsymbol{T}} \\ \boldsymbol{G_w} &= \left[[\mathrm{N}_w](\xi_1) \quad [\mathrm{N}_w](\xi_2) \quad \ldots\ldots \quad [\mathrm{N}_w](\xi_N)\right]^{\boldsymbol{T}} \end{aligned} \tag{66}$$

By replacing Eqs. (41), (43), (44), (64) and (66) in the deformation and kinetic energy Eqs. (28)-(32), and (38), and using the Lagrangian equation formula, the elementary mass, and stiffness matrix are obtained as:

The elementary mass matrix obtained with (DQHFEM)

$$[M^e] = \begin{bmatrix} [M^e]_{11} & [M^e]_{12} & [M^e]_{13} \\ & [M^e]_{22} & [M^e]_{23} \\ sym & & [M^e]_{33} \end{bmatrix} \tag{67}$$

Hence the components of the elementary mass matrix are detailed in the annex.

The stiffness matrices obtained with (DQHFEM)

$$[K_\varepsilon^e] = \begin{bmatrix} [K_\varepsilon^e]_{11} & [K_\varepsilon^e]_{12} & [K_\varepsilon^e]_{13} \\ & [K_\varepsilon^e]_{22} & [K_\varepsilon^e]_{23} \\ sym & & [K_\varepsilon^e]_{33} \end{bmatrix} \tag{68}$$

$$\left[K_\gamma^e\right] = \begin{bmatrix} \left[K_\gamma^e\right]_{11} & \left[K_\gamma^e\right]_{12} & \left[K_\gamma^e\right]_{13} \\ & \left[K_\gamma^e\right]_{22} & \left[K_\gamma^e\right]_{23} \\ sym & & \left[K_\gamma^e\right]_{33} \end{bmatrix} \tag{69}$$

$$[K_\eta^e] = \begin{bmatrix} [K_\eta^e]_{11} & [K_\eta^e]_{12} & [K_\eta^e]_{13} \\ & [K_\eta^e]_{22} & [K_\eta^e]_{23} \\ sym & & [K_\eta^e]_{33} \end{bmatrix} \tag{70}$$

$$[K_\chi^e] = \begin{bmatrix} [0] & [0] & [0] \\ & [K_\chi^e]_{22} & [K_\chi^e]_{23} \\ sym & & [K_\chi^e]_{33} \end{bmatrix} \tag{71}$$

With $[K_\varepsilon^e], [K_\gamma^e], [K_\eta^e]$ and $[K_\chi^e]$ are, respectively, the elementary deformation, expansion gradient, deviatoric stretching gradient, and rotationally symmetric gradient matrices.

Hence the components of the elementary deformation matrices are detailed in the appendix.

All knot distribution shapes for differencing and squaring are [-1, 1]. Therefore, in order to apply them in practice, the following modifications must be made to the differentiation and quadrature matrices

$$\overline{\boldsymbol{C}} = \frac{l_e}{2} C, \quad \overline{\boldsymbol{A}}^{(1)} = \frac{2}{l_e} A^{(1)}, \quad \overline{\boldsymbol{A}}^{(2)} = \frac{4}{{l_e}^2} A^{(2)}, \quad \overline{\boldsymbol{A}}^{(3)} = \frac{8}{{l_e}^3} A^{(3)} \tag{72}$$

Where l_e is the length of the beam element.

The matrices for the entire system are obtained according to the MEF rules for assembling elementary matrices

$$([K] - \omega^2[M])A_{mp} = [0] \tag{73}$$

3. Discussion of results

A microbeam made of porous foam metal shown in Fig. 1, and a homogeneous microbeam are studied in this section. The material properties for the porous microbeam are: Young's modulus $E_1 = 200$ GPa, a mass density $\rho_1 = 7850$ Kg/m^3, Poisson's ratio $\nu = 0.33$, and the material length scale parameters $l = 17.6$ μm. The width/thickness ratio for this case is $b/h = 2$.

For the homogeneous microbeam case, the material properties taken are: Young's modulus $E = 1.44$ GPa, a mass density $\rho = 1220$ Kg/m^3, Poisson's ratio $\nu = 0.38$, the material length scale parameters $l = 17.6$ μm, and the ratio The width/thickness ratio for this case is $b/h = 2$. The parameters of the material length scale are equal to $l_0 = l_1 = l_2 = l$ for the MSGT case, in the CT case all material length scale parameters are zero $l_0 = l_1 = l_2 = 0$, and in the MCST case $l_0 = l_1 = 0$ and $l_2 \neq 0$.

In order to examine the current models, a comparative search is first carried out with the literature. For the homogeneous microbeam (Akgöz and Civalek 2013, Wang *et al.* 2018), and for the porous microbeam (Wang *et al.* 2018).

The following nondimensional parameters are introduced to simplify the results

$$\omega^* = \omega L^2 \sqrt{\frac{\int_{-h/2}^{h/2} \rho \, dz}{\int_{-h/2}^{h/2} E \, z^2 \, dz}} \tag{74}$$

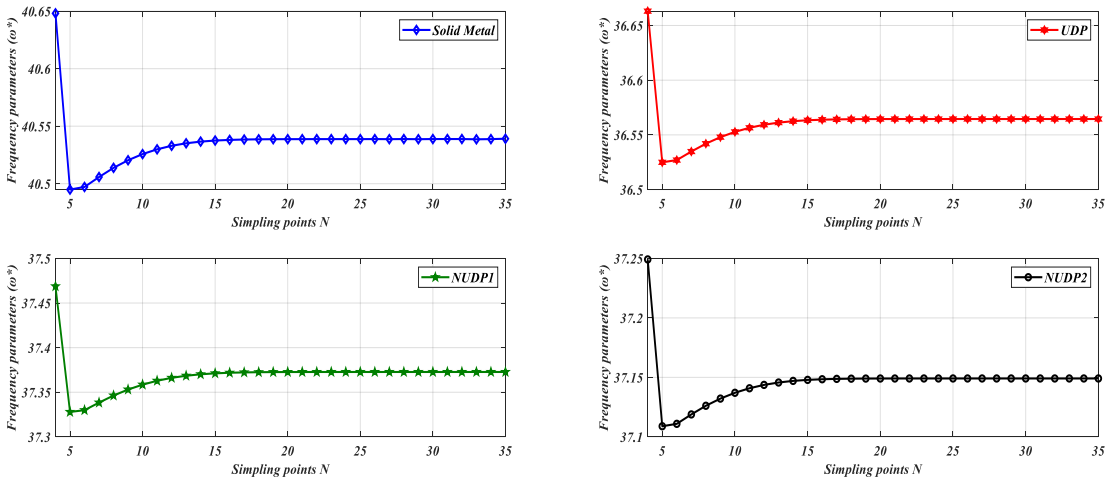

Fig. 5 First mode convergence, for various forms models of porosity distributions ($h = l,\ L = 10h,\ e_0 = 0.5$)

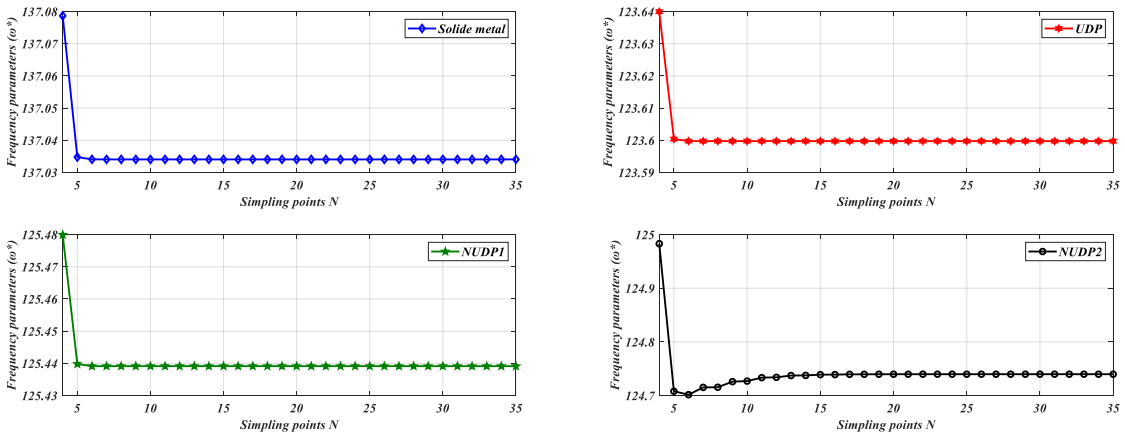

Fig. 6 Second mode convergence, for various forms models of porosity distributions ($h = l, L = 10h, e_0 = 0.5$)

3.1 Convergence

From the convergence results in Figs. 5-6, we can see that the frequency parameters converge quickly, which demonstrate the efficacy of the resolution approach used, and to ensure a good validation with the literature. In the following, we will choose a number of sampling N=20. Because according to the convergence results the frequency parameters have already been converged.

3.2 Validation

In a first validation, for a homogenous microbeam, a comparison of natural nondimensional frequencies is made. Simply supported in both edges.

Table 1 Non-dimensional fundamental frequencies first mode

h/l	Theory	*L*=10h			*L*=30h			*L*=100h		
		CT	MCST	MSGT	CT	MCST	MSGT	CT	MCST	MSGT
1	(Akgöz and Civalek 2013)	13.1239	24.3157	40.3106	13.4595	24.5801	40.8962	13.4996	24.6112	40.9659
	(Wang *et al.* 2018)			40.3106			40.8962			40.9659
	Present	13.3857	23.3053	40.3190	13.4903	24.4564	40.8931	13.5024	24.6000	40.9655
5	(Akgöz and Civalek 2013)	13.1239	13.7542	15.1796	13.4595	14.0749	15.5184	13.4996	14.1132	15.5589
	(Wang *et al.* 2018)			15.1796			15.5184			15.5589
	Present	13.3857	13.9722	15.3986	13.4903	14.1006	15.5441	13.5024	14.1155	15.5612
10	(Akgöz and Civalek 2013)	13.1239	13.2844	13.6670	13.4595	13.6160	14.0027	13.4996	13.6556	14.0428
	(Wang *et al.* 2018)			13.6670			14.0027			14.0428
	Present	13.3857	13.5352	13.9170	13.4903	13.6455	14.0320	13.5024	13.6583	14.0455

Table 2 Non-dimensional fundamental frequencies for second mode

h/l	Theory	*L*=10h			*L*=30h			*L*=100h		
		CT	MCST	MSGT	CT	MCST	MSGT	CT	MCST	MSGT
1	(Akgöz and Civalek 2013)	48.6922	94.1134	154.5577	53.3206	97.9163	162.6833	53.9507	98.4080	163.7807
	(Wang *et al.* 2018)			154.5577			162.6833			163.7807
	Present	52.2237	81.8122	152.8290	53.8027	96.0096	162.6629	53.9953	98.2283	163.7743
5	(Akgöz and Civalek 2013)	48.6922	51.3623	56.8752	53.3206	55.8057	61.5514	53.9507	56.4071	62.1874
	(Wang *et al.* 2018)			56.8752			61.5514			62.1874
	Present	52.2237	54.2862	59.8753	53.8027	56.2075	61.9549	53.9953	56.4442	62.2244
10	(Akgöz and Civalek 2013)	48.6922	49.3752	50.8635	53.3206	53.9529	55.4932	53.9507	54.5752	56.1234
	(Wang *et al.* 2018)			50.8635			55.4932			56.1234
	Present	52.2237	52.7532	54.2390	53.8027	54.4147	55.9529	53.9953	54.6179	56.1658

For the validation of the accuracy of the results obtained in this work with other research works in the literature, Tables 1-2 presenting the results provided from the current DQHFEM method compared with the analytical used in the works (Akgöz and Civalek 2013) and (Wang *et al.* 2018), for a homogeneous microbeam. The second validation, is done for a porous metal foam microbeam, Table 3 compares the results of the present DQHFEM method to the analytical approaches used in the study (Wang *et al.* 2018). As can be seen, the current tabulated results and those published in the open literature are quite similar, with only a little percentage difference, suggesting that the resolution approach utilized in this investigation was correct.

Tables 1 and 2 show that CT predicts lower dimensions natural frequencies than the others, but MSGT predicts higher dimensional natural frequencies. Furthermore, as the h/l ratio rises, the difference between the non-dimensional natural frequencies corresponding to the classical and non-classical models decreases, and this difference is bigger for higher modes.

Table 3 Comparison of porous microbeam's non-dimensional natural frequencies. (MSGT) ($h = l$, $e_0 = 0.5$)

Mode	L/h		Solid metal	UPD	NUDP1	NUDP2
01	10	Present	40.5387	36.5645	37.3727	37.1491
		(Wang *et al.* 2018)	40.5569	36.5808	37.4324	37.1877
	30	Present	41.1148	37.0840	37.9505	37.6853
		(Wang *et al.* 2018)	41.1210	37.0896	37.9617	37.7066
	100	Present	41.1874	37.1496	38.0236	37.7528
		(Wang *et al.* 2018)	41.1881	37.1502	38.0248	37.7684
02	10	Present	156.0761	140.7749	143.4398	143.3775
		(Wang *et al.* 2018)	155.764	140.494	143.687	142.809
	30	Present	163.5465	147.5130	150.8845	149.6080
		(Wang *et al.* 2018)	163.616	147.576	151.032	150.028
	100	Present	164.6615	148.5187	152.0057	150.6734
		(Wang *et al.* 2018)	164.673	148.529	152.024	151.000

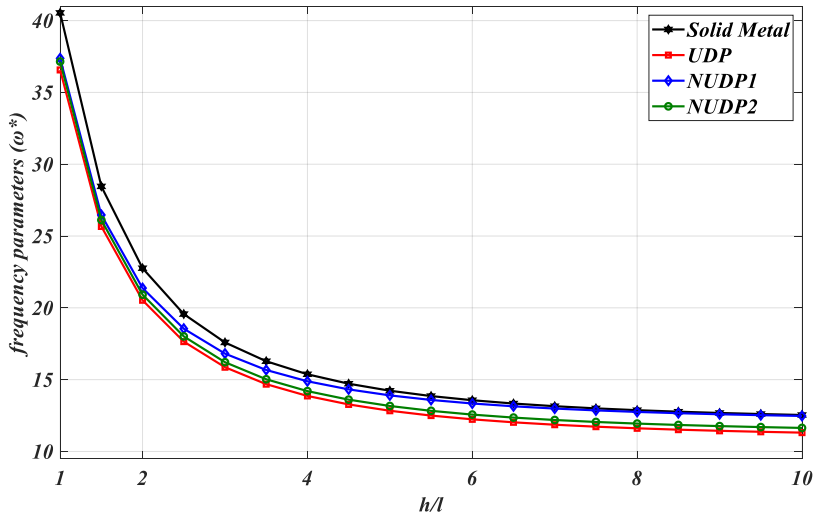

Fig. 7 Frequency parameters ω^* for various porosity distributions as a function of thickness (e_0=0.5, L=10h) (MSGT)

3.3 Parametric study

In this section, a parametric study will be provided to study the influence of some geometrical and physical parameters on the maximum value of the dimensionless frequency ω^*, such as the scale length, the nature of the material porosity distribution, and other.

For different forms of porosity distributions, Fig. 7 displays the frequency parameters versus to the ratio of the microbeam thickness and parameter of material length scale. The results in this figure, clearly show that the frequency parameters decrease with increasing value of the ratio of the microbeam thickness and the material length scale parameter h/l. The deviation of the frequency parameters between the different types of porosity distribution is small for small values of the h/l ratio. This indicates that the impact of the distribution model of the porosity is important

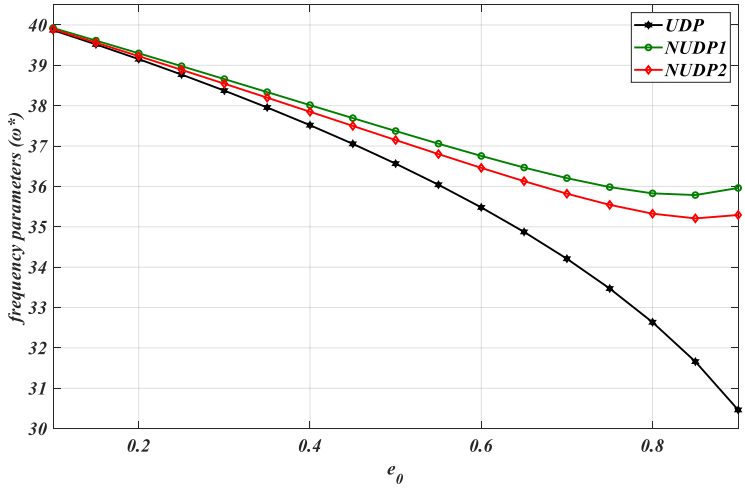

Fig. 8 Frequency parameters ω^* for various porosity distributions as a function of porosity coefficient (h/l=1, L=10h) (MSGT)

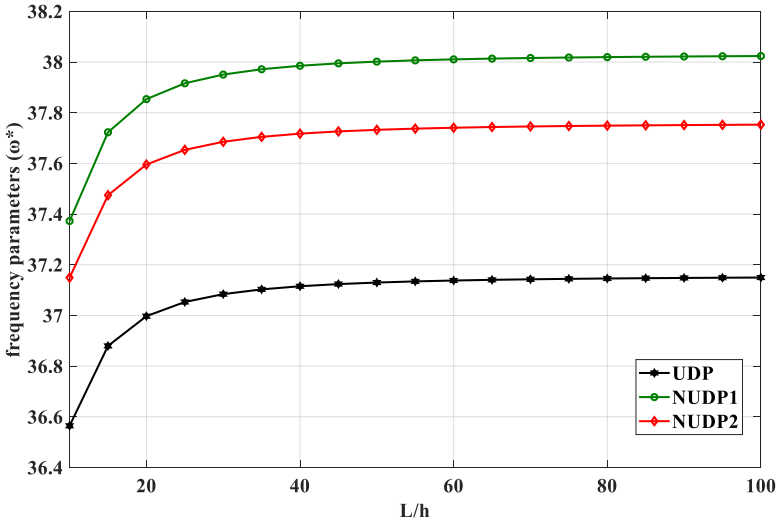

Fig. 9 Frequency parameters ω^* according to length/thickness ratio for various porosity distributions (h/l=1, e_0=0.5) (MSGT)

for thick microbeams.

Fig. 8 shows the variation of the frequency parameters against the porosity coefficient, for different types of porosity distributions. It can be seen that the values of the frequency parameters decrease as the value of the porosity coefficient increases. And this is explained physically, that the stiffness and the mass density decrease by increasing the porosity coefficient, and that the stiffness is largely reduced compared to the mass density.

The results in Fig. 8 also show, that for a low value of porosity coefficient, the deviation between the frequency parameters for different type of porosity distribution is largely small,

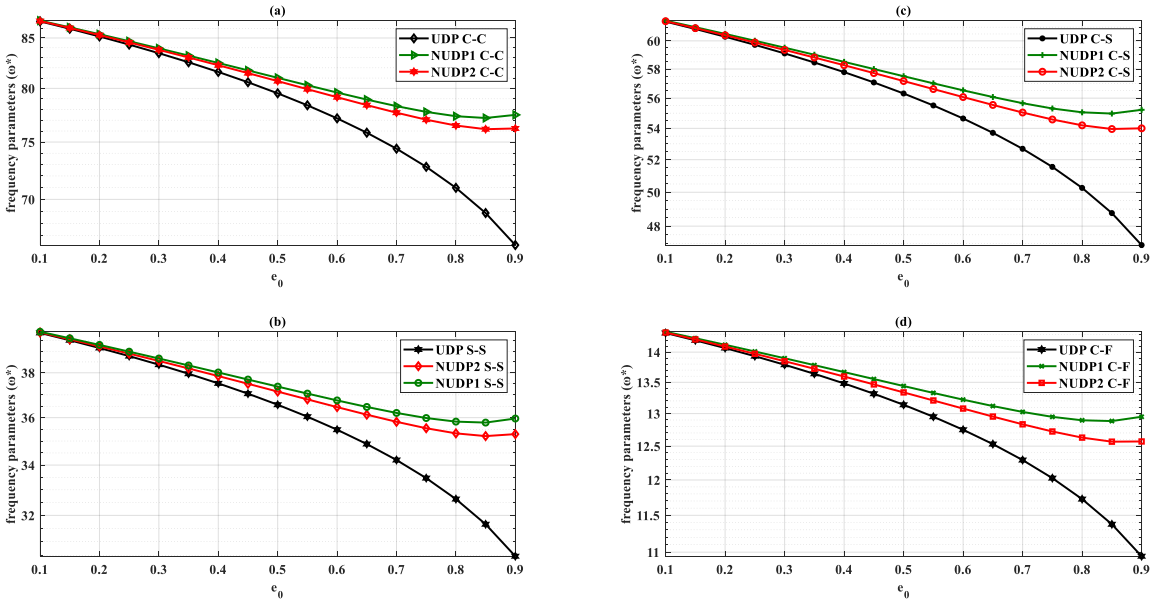

Fig. 10 Frequency parameters ω^* for various porosity distributions based on porosity coefficient (h/l=1, L=10 h, b/h=2) (MSGT), (a) Clamped-Clamped, (b) Simply Supported-Simply supported (c) Clamped-Simply supported, (d) Clamped-Free.

however, as the porosity coefficient rises, this deviation grows more and higher.

It can also be seen that the UDP type microbeam is very different from the NUDP1 and NUDP2 microbeams. The frequency parameter value continued to decrease with the increase of the porosity coefficient, while in the case of the NUDP1 and NUDP2 microbeams, the frequency parameter values initially decrease and then at a certain porosity coefficient value they start to increase.

Fig. 9 shows the frequency parameters versus slenderness ratio for different types of microbeam porosity distributions. We can also see that the frequency parameter's value increases quickly at small length-to-thickness ratios, but varies slightly when L/h>50. This means that when the length-to-thickness ratio is small, the frequency parameter of porous microbeams is affected significantly.

Fig. 10 shows the frequency parameters as a function of porosity coefficient, for different types of porosity distribution and boundary conditions, (a): Clamped-Clamped, (b): Simply Supported-Simply supported, (c): Clamped- Simply supported, (d): Clamped-Free. According to the results, one can see that an increment in the value of porosity parameter $\boldsymbol{e_0}$ leads to a reduction in the nondimensional frequency, and that for all types of end supports conditions. Furthermore, we notice that the boundary conditions have a large influence on the frequency parameters, the C-C boundary condition type gives a large value of frequency parameter, followed by C-S, S-S and C-F, respectively due to stiffening effect of the support, and the C-F graded material porous microbeam has the smallest fundamental frequency than other supports.

For a porous microbeam with a UDP distribution model, Figs. 11, 12 and 13 show the influence of the porosity coefficient and the thickness-material length (h/l) scale parameter ratio of microbeam on the natural frequency parameter. The natural frequencies based on MSGT are

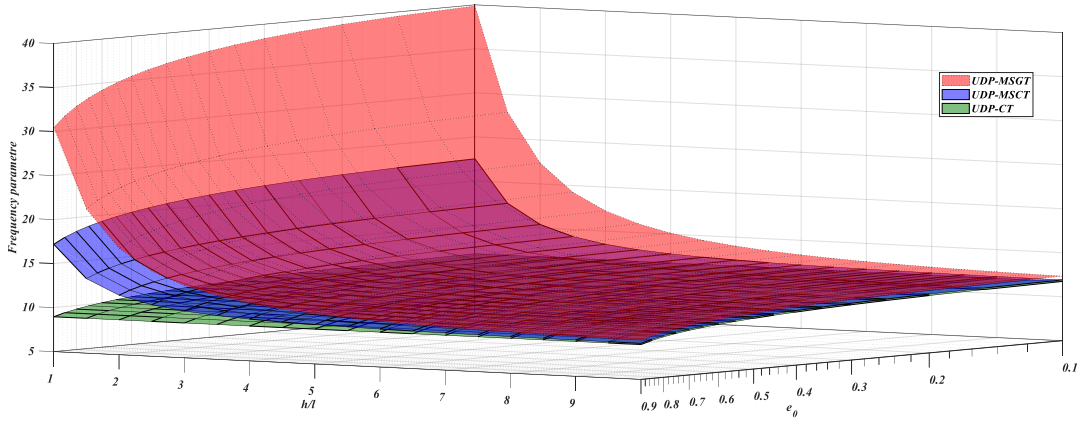

Fig. 11 First frequencies parameters with respect to the porosity distribution and the thickness-material length scale parameter ratio (L/h=10, b/h=2. Porosity distribution UDP)

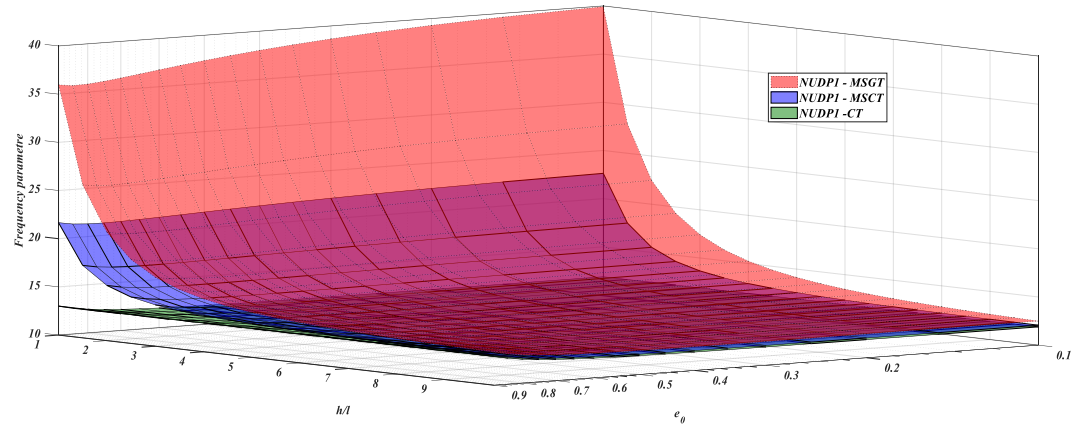

Fig. 12 First frequencies parameters with respect to the porosity distribution and the thickness-material length scale parameter ratio (L/h=10, b/h=2. Porosity distribution NUDP1)

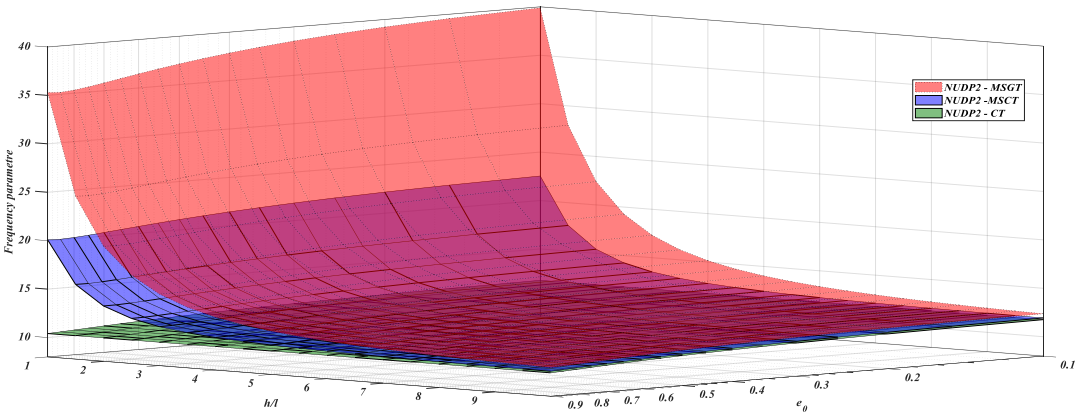

Fig. 13 First frequencies parameters with respect to the porosity distribution and the thickness-material length scale parameter ratio (L/h=10, b/h=2. Porosity distribution NUDP2)

always larger than CT and MCST, regardless of the porosity distribution model, as demonstrated in Figs. 12 and 13 for the NUDP1 and NUDP2 models, respectively. Moreover, from these figures we notice that the influence of

h/l ratio on the maximum values of natural frequencies is significantly important when the value of this parameter is in range of 1 and 4, in which the variation shape take a nonlinear variation due to the significant stiffness drop for the FG microstructure, and this for the three cases provided considering: MSGT, MSCT and CT. Furthermore, it is seen that by increasing the h/l ratio the gap becomes small between MSGT, CT and MSCT because of the last one has more length scale parameter compared to others and can capture the size dependency more efficiently. In addition, from the Figs. 11, 12 and 13 it is shown that the natural frequency of the FG porous microbeam decreases as the porosity coefficient increases with no noticeable difference between the three micro size dependency models. This phenomenon occurs because increasing the porosity coefficient reduces both stiffness and mass density, with the stiffness reduction being significantly greater than the mass density reduction.

4. Conclusions

In this paper we have presented an analysis on the dynamic free vibration response of a porous microbeam based on the refined high order beam deformation theory, with sinusoidal shear deformation function in conjunction with the modified gradient deformation theory MSGT. The Lagrange principle is used with the hierarchical deferential quadrature finite element method DQHFEM to obtain the governing equations. Three kinds of porosity distribution models UDP, NUDP1, and NUDP2 were considered to see their effects on the maximum value of the non-dimensional frequency. The results are compared with analytical results in the literature to show the effectiveness of the provided numerical resolution procedure. The numerical results in this work led us to conclude that:

- The actual numerical method based on DQHFEM gives precise results and very close to the analytical results found in the literature with fast convergence rate, which confirms its effectiveness.
- Microbeams that are based on non-classical theories, such as MSGT, are more rigid than those that are based on classical theory, which explains why the frequencies for the MSGT case are large compared to those for the CT case.
- If there is only one material length scaling parameter ($l_0 = l_1 = 0,\ l_2 = l$), the present non-classical model based on MSGT will become another non-classical model based on MCST. Furthermore, if all material length scale parameters are equal to zero ($l_0 = l_1 = l_2 = 0$), the current non-classical model will become a classical model.
- Natural frequencies of porous microbeams are lower than those of solid metallic microbeams. With a high coefficient of porosity and microbeam thickness, the porosity shape distribution has a substantial impact on the natural frequency.
- The present numerical method can easily administer mixed boundary conditions, for dynamic study of macro/micro structure.
- The natural frequencies of the UDP porous microbeam degrade as the porosity coefficient increase, whereas for the NUPD 1 and NUPD 2 porous microbeams, they initially reduce and then increase as the porosity coefficient increases.
- The length-to-thickness ratio (L/h) has a significant effect on the natural frequencies, where

an increase in its value will lead to an increase in the magnitude of the frequency parameter.
• The UPD always corresponds to the lowest frequency among the various forms of porosity distribution. Natural frequency differences between the UPD and the other two are rather evident. On the other hand, the FG NUPD 1 microbeam natural frequencies are a bit higher compared to those of the NUPD 2 microbeam.

Acknowledgements

We acknowledge with grateful thanks the support by the laboratory of mechanical and material systems engineering (IS2M) in university of Tlemcen, as well as the General Directorate of Scientific Research and Technological Development (DGRSDT) of the Ministry of Higher Education of Algeria.

References

Abdelrahman, A. A., Esen, I., & Eltaher, M. A. (2021). Vibration response of Timoshenko perforated microbeams under accelerating load and thermal environment. *Applied Mathematics and Computation*, *407*, 126307. https://doi.org/https://doi.org/10.1016/j.amc.2021.126307

Ahmed, S., Abdelhamid, H., Ismail, B., & Ahmed, F. (2020). An Differential Quadrature Finite Element and the Differential Quadrature Hierarchical Finite Element Methods for the Dynamics Analysis of on Board Shaft. *European Journal of Computational Mechanics*, *29*(4-6), 303–344. https://doi.org/10.13052/ejcm1779-7179.29461

Akgöz, B., & Civalek, Ö. (2013). A size-dependent shear deformation beam model based on the strain gradient elasticity theory. *International Journal of Engineering Science*, *70*, 1-14. https://doi.org/https://doi.org/10.1016/j.ijengsci.2013.04.004

Assem, H., Hadjoui, A., & Saimi, A. (2022). Numerical analysis on the dynamics behavior of FGM rotor in thermal environment using h-p finite element method. *Mechanics Based Design of Structures and Machines*, *50*(11), 3925-3948. https://doi.org/10.1080/15397734.2020.1824791

Aydogdu, M. (2009). A general nonlocal beam theory: Its application to nanobeam bending, buckling and vibration. *Physica E: Low-dimensional Systems and Nanostructures*, *41*(9), 1651-1655. https://doi.org/https://doi.org/10.1016/j.physe.2009.05.014

Barati, M. R., & Zenkour, A. M. (2017). Investigating post-buckling of geometrically imperfect metal foam nanobeams with symmetric and asymmetric porosity distributions. *Composite Structures*, *182*, 91-98. https://doi.org/https://doi.org/10.1016/j.compstruct.2017.09.008

Bardell, N. S. (1996). An engineering application of the h-p Version of the finite element method to the static analysis of a Euler-Bernoulli beam. *Computers & Structures*, *59*(2), 195-211. https://doi.org/https://doi.org/10.1016/0045-7949(95)00252-9

Bensaid, I., & Guenanou, A. (2017). Bending and stability analysis of size-dependent compositionally graded Timoshenko nanobeams with porosities. *Advances in materials Research*, *6*(1), 45-63. https://doi.org/10.12989/AMR.2017.6.1.045

Bensaid, I., & Saimi, A. (2022). Dynamic investigation of functionally graded porous beams resting on viscoelastic foundation using generalised differential quadrature method. *Australian Journal of Mechanical Engineering*, 1-20. https://doi.org/10.1080/14484846.2021.2017115

Bensaid, I., Saimi, A., & Civalek, Ö. (2022). Effect of two-dimensional material distribution on dynamic and buckling responses of graded ceramic-metal higher order beams with stretch effect. *Mechanics of Advanced Materials and Structures*, 1-17. https://doi.org/10.1080/15376494.2022.2142342

Chai, Q., & Wang, Y. Q. (2022). Traveling wave vibration of graphene platelet reinforced porous joined

conical-cylindrical shells in a spinning motion. *Engineering Structures*, *252*, 113718. https://doi.org/https://doi.org/10.1016/j.engstruct.2021.113718

Chen, D., Kitipornchai, S., & Yang, J. (2016). Nonlinear free vibration of shear deformable sandwich beam with a functionally graded porous core. *Thin-Walled Structures*, *107*, 39-48. https://doi.org/https://doi.org/10.1016/j.tws.2016.05.025

Chen, D., Yang, J., & Kitipornchai, S. (2015). Elastic buckling and static bending of shear deformable functionally graded porous beam. *Composite Structures*, *133*, 54-61. https://doi.org/https://doi.org/10.1016/j.compstruct.2015.07.052

Ebrahimi, F., & Jafari, A. (2018). A four-variable refined shear-deformation beam theory for thermo-mechanical vibration analysis of temperature-dependent FGM beams with porosities. *Mechanics of Advanced Materials and Structures*, *25*(3), 212-224. https://doi.org/10.1080/15376494.2016.1255820

Ebrahimi, F., Mahmoodi, F., & Barati, M. R. (2017). Thermo-mechanical vibration analysis of functionally graded micro/nanoscale beams with porosities based on modified couple stress theory. *Advances in materials Research*, *6*(3), 279.

Fleck, N. A., Muller, G. M., Ashby, M. F., & Hutchinson, J. W. (1994). Strain gradient plasticity: Theory and experiment. *Acta Metallurgica et Materialia*, *42*(2), 475-487. https://doi.org/https://doi.org/10.1016/0956-7151(94)90502-9

Ihab Eddine, H., Ismail, B., Ahmed, S., & Abdelmadjid, C. (2023). Free Vibration Analysis of Functionally Graded Carbon Nanotube-Reinforced Higher Order Refined Composite Beams Using Differential Quadrature Finite Element Method. *European Journal of Computational Mechanics*, *31*(4), 1-34. https://doi.org/10.13052/ejcm2642-2085.3143

Jabbari, M., Mojahedin, A., Khorshidvand, A. R., & Eslami, M. R. (2014). Buckling Analysis of a Functionally Graded Thin Circular Plate Made of Saturated Porous Materials. *Journal of Engineering Mechanics*, *140*(2), 287-295. https://doi.org/doi:10.1061/(ASCE)EM.1943-7889.0000663

Jalaei, M. H., Thai, H. T., & Civalek, Ö. (2022). On viscoelastic transient response of magnetically imperfect functionally graded nanobeams. *International Journal of Engineering Science*, *172*, 103629. https://doi.org/https://doi.org/10.1016/j.ijengsci.2022.103629

Karamanli, A., & Aydogdu, M. (2019). On the vibration of size dependent rotating laminated composite and sandwich microbeams via a transverse shear-normal deformation theory. *Composite Structures*, *216*, 290-300. https://doi.org/https://doi.org/10.1016/j.compstruct.2019.02.044

Karamanli, A., & Aydogdu, M. (2020). Vibration of functionally graded shear and normal deformable porous microplates via finite element method. *Composite Structures*, *237*, 111934. https://doi.org/https://doi.org/10.1016/j.compstruct.2020.111934

Karamanli, A., Aydogdu, M., & Vo, T. P. (2021). A comprehensive study on the size-dependent analysis of strain gradient multi-directional functionally graded microplates via finite element model. *Aerospace Science and Technology*, *111*, 106550. https://doi.org/https://doi.org/10.1016/j.ast.2021.106550

Karamanli, A., & Vo, T. P. (2021a). Bending, vibration, buckling analysis of bi-directional FG porous microbeams with a variable material length scale parameter. *Applied Mathematical Modelling*, *91*, 723-748. https://doi.org/https://doi.org/10.1016/j.apm.2020.09.058

Karamanli, A., & Vo, T. P. (2021b). A quasi-3D theory for functionally graded porous microbeams based on the modified strain gradient theory. *Composite Structures*, *257*, 113066. https://doi.org/https://doi.org/10.1016/j.compstruct.2020.113066

Karamanli, A., Vo, T. P., & Civalek, O. (2022). Finite element formulation of metal foam microbeams via modified strain gradient theory. *Engineering with Computers*. https://doi.org/10.1007/s00366-022-01666-x

Ke, L.-L., Wang, Y.-S., & Wang, Z.-D. (2011). Thermal effect on free vibration and buckling of size-dependent microbeams. *Physica E: Low-dimensional Systems and Nanostructures*, *43*(7), 1387-1393. https://doi.org/https://doi.org/10.1016/j.physe.2011.03.009

Lam, D. C. C., Yang, F., Chong, A. C. M., Wang, J., & Tong, P. (2003). Experiments and theory in strain gradient elasticity. *Journal of the Mechanics and Physics of Solids*, *51*(8), 1477-1508. https://doi.org/https://doi.org/10.1016/S0022-5096(03)00053-X

Li, Y. S., Feng, W. J., & Cai, Z. Y. (2014). Bending and free vibration of functionally graded piezoelectric beam based on modified strain gradient theory. *Composite Structures*, *115*, 41-50. https://doi.org/https://doi.org/10.1016/j.compstruct.2014.04.005

Lim, C. W., Zhang, G., & Reddy, J. N. (2015). A higher-order nonlocal elasticity and strain gradient theory and its applications in wave propagation. *Journal of the Mechanics and Physics of Solids*, *78*, 298-313. https://doi.org/https://doi.org/10.1016/j.jmps.2015.02.001

Liu, C., Liu, B., Zhao, L., Xing, Y., Ma, C., & Li, H. (2017). A differential quadrature hierarchical finite element method and its applications to vibration and bending of Mindlin plates with curvilinear domains. *International Journal for Numerical Methods in Engineering*, *109*(2), 174-197. https://doi.org/https://doi.org/10.1002/nme.5277

Mindlin, R. D. (1965). Second gradient of strain and surface-tension in linear elasticity. *International Journal of Solids and Structures*, *1*(4), 417-438. https://doi.org/https://doi.org/10.1016/0020-7683(65)90006-5

Mirsalehi, M., Azhari, M., & Amoushahi, H. (2017). Buckling and free vibration of the FGM thin micro-plate based on the modified strain gradient theory and the spline finite strip method. *European Journal of Mechanics - A/Solids*, *61*, 1-13. https://doi.org/https://doi.org/10.1016/j.euromechsol.2016.08.008

Nguyen, N.-D., Nguyen, T.-N., Nguyen, T.-K., & Vo, T. P. (2022). A new two-variable shear deformation theory for bending, free vibration and buckling analysis of functionally graded porous beams. *Composite Structures*, *282*, 115095. https://doi.org/https://doi.org/10.1016/j.compstruct.2021.115095

Peano, A. (1976). Hierarchies of conforming finite elements for plane elasticity and plate bending. *Computers & Mathematics with Applications*, *2*(3), 211-224. https://doi.org/https://doi.org/10.1016/0898-1221(76)90014-6

Rezaei, A. S., & Saidi, A. R. (2016). Application of Carrera Unified Formulation to study the effect of porosity on natural frequencies of thick porous–cellular plates. *Composites Part B: Engineering*, *91*, 361-370. https://doi.org/https://doi.org/10.1016/j.compositesb.2015.12.050

Saimi, A., Fellah, A., & Hadjoui, A. (2021). Nonlinear dynamic analysis of the response to the excitation forces of a symmetrical on-board rotor mounted on hydrodynamic bearings using h-p finite elements method. *Mechanics Based Design of Structures and Machines*, 1-32. https://doi.org/10.1080/15397734.2021.1991806

Saimi, A., & Hadjoui, A. (2016). An engineering application of the h-p version of the finite elements method to the dynamics analysis of a symmetrical on-board rotor. *European Journal of Computational Mechanics*, *25*(5), 388-416. https://doi.org/10.1080/17797179.2016.1245597

Şimşek, M., & Reddy, J. N. (2013). Bending and vibration of functionally graded microbeams using a new higher order beam theory and the modified couple stress theory. *International Journal of Engineering Science*, *64*, 37-53. https://doi.org/https://doi.org/10.1016/j.ijengsci.2012.12.002

Stölken, J. S., & Evans, A. G. (1998). A microbend test method for measuring the plasticity length scale. *Acta Materialia*, *46*(14), 5109-5115. https://doi.org/https://doi.org/10.1016/S1359-6454(98)00153-0

Teng, M. W., & Wang, Y. Q. (2021). Nonlinear forced vibration of simply supported functionally graded porous nanocomposite thin plates reinforced with graphene platelets. *Thin-Walled Structures*, *164*, 107799. https://doi.org/https://doi.org/10.1016/j.tws.2021.107799

Thai, H.-T., & Vo, T. P. (2012). Bending and free vibration of functionally graded beams using various higher-order shear deformation beam theories. *International Journal of Mechanical Sciences*, *62*(1), 57-66. https://doi.org/https://doi.org/10.1016/j.ijmecsci.2012.05.014

Thai, S., Thai, H.-T., Vo, T. P., & Patel, V. I. (2017). Size-dependant behaviour of functionally graded microplates based on the modified strain gradient elasticity theory and isogeometric analysis. *Computers & Structures*, *190*, 219-241. https://doi.org/https://doi.org/10.1016/j.compstruc.2017.05.014

Thang, P. T., Nguyen-Thoi, T., Lee, D., Kang, J., & Lee, J. (2018). Elastic buckling and free vibration analyses of porous-cellular plates with uniform and non-uniform porosity distributions. *Aerospace Science and Technology*, *79*, 278-287. https://doi.org/https://doi.org/10.1016/j.ast.2018.06.010

Touratier, M. (1991). An efficient standard plate theory. *International Journal of Engineering Science*, *29*(8), 901-916.

Wang, C. M., Kitipornchai, S., Lim, C. W., & Eisenberger, M. (2008). Beam Bending Solutions Based on Nonlocal Timoshenko Beam Theory. *Journal of Engineering Mechanics*, *134*(6), 475-481. https://doi.org/doi:10.1061/(ASCE)0733-9399(2008)134:6(475)

Wang, Y. Q. (2018). Electro-mechanical vibration analysis of functionally graded piezoelectric porous plates in the translation state. *Acta Astronautica*, *143*, 263-271. https://doi.org/https://doi.org/10.1016/j.actaastro.2017.12.004

Wang, Y. Q., Ye, C., & Zu, J. W. (2019). Nonlinear vibration of metal foam cylindrical shells reinforced with graphene platelets. *Aerospace Science and Technology*, *85*, 359-370. https://doi.org/https://doi.org/10.1016/j.ast.2018.12.022

Wang, Y. Q., Zhao, H. L., Ye, C., & Zu, J. W. (2018). A Porous Microbeam Model for Bending and Vibration Analysis Based on the Sinusoidal Beam Theory and Modified Strain Gradient Theory. *International Journal of Applied Mechanics*, *10*(05), 1850059. https://doi.org/10.1142/s175882511850059x

Wang, Y. Q., Zhao, H. L., & Zu, C. Y. a. J. W. (2018). A Porous Microbeam Model for Bending and Vibration Analysis Based on the Sinusoidal Beam Theory and Modified Strain Gradient Theory. *International Journal of Applied Mechanics*, *10*(5), 1850059.

Wang, Y. Q., & Zu, J. W. (2017). Vibration behaviors of functionally graded rectangular plates with porosities and moving in thermal environment. *Aerospace Science and Technology*, *69*, 550-562. https://doi.org/https://doi.org/10.1016/j.ast.2017.07.023

Wattanasakulpong, N., Gangadhara Prusty, B., Kelly, D. W., & Hoffman, M. (2012). Free vibration analysis of layered functionally graded beams with experimental validation. *Materials & Design (1980-2015)*, *36*, 182-190. https://doi.org/https://doi.org/10.1016/j.matdes.2011.10.049

Wattanasakulpong, N., & Ungbhakorn, V. (2014). Linear and nonlinear vibration analysis of elastically restrained ends FGM beams with porosities. *Aerospace Science and Technology*, *32*(1), 111-120. https://doi.org/https://doi.org/10.1016/j.ast.2013.12.002

Xing, Y., & Liu, B. (2009). High-accuracy differential quadrature finite element method and its application to free vibrations of thin plate with curvilinear domain. *International Journal for Numerical Methods in Engineering*, *80*(13), 1718-1742. https://doi.org/https://doi.org/10.1002/nme.2685

Xu, H., Wang, Y. Q., & Zhang, Y. (2021). Free vibration of functionally graded graphene platelet-reinforced porous beams with spinning movement via differential transformation method. *Archive of Applied Mechanics*, *91*(12), 4817-4834. https://doi.org/10.1007/s00419-021-02036-7

Yang, F., Chong, A. C. M., Lam, D. C. C., & Tong, P. (2002). Couple stress based strain gradient theory for elasticity. *International Journal of Solids and Structures*, *39*(10), 2731-2743. https://doi.org/https://doi.org/10.1016/S0020-7683(02)00152-X

Ye, C., & Wang, Y. Q. (2021). Nonlinear forced vibration of functionally graded graphene platelet-reinforced metal foam cylindrical shells: internal resonances. *Nonlinear Dynamics*, *104*(3), 2051-2069. https://doi.org/10.1007/s11071-021-06401-7

CC

Appendix

Component of the elementary mass matrix

$$\begin{cases} [M^e]_{11} = J_1[G^T\bar{C}G] \\ [M^e]_{12} = -J_2\left[G^T\bar{C}\bar{A}^{(1)}G\right] \\ [M^e]_{13} = J_3\left[G^T\bar{C}\bar{A}^{(1)}G\right] \\ [M^e]_{22} = J_1[G^T\bar{C}G] + J_5\left[G^T\bar{A}^{(1)^T}\bar{C}\bar{A}^{(1)}G\right] \\ [M^e]_{23} = J_1[G^T\bar{C}G] - J_4\left[G^T\bar{A}^{(1)^T}\bar{C}\bar{A}^{(1)}G\right] \\ [M^e]_{33} = J_1[G^T\bar{C}G] + J_6\left[G^T\bar{A}^{(1)^T}\bar{C}\bar{A}^{(1)}G\right] \end{cases} \tag{75}$$

The components of the elementary strain matrices

$$\begin{cases} [K_\varepsilon^e]_{11} = I_1\left[G^T\bar{A}^{(1)^T}\bar{C}\bar{A}^{(1)}G\right] \\ [K_\varepsilon^e]_{12} = -I_2\left[G^T\bar{A}^{(1)^T}\bar{C}\bar{A}^{(2)}G\right] \\ [K_\varepsilon^e]_{13} = I_3\left[G^T\bar{A}^{(1)^T}\bar{C}\bar{A}^{(2)}G\right] \\ [K_\varepsilon^e]_{22} = I_5\left[G^T\bar{A}^{(2)^T}\bar{C}\bar{A}^{(2)}G\right] \\ [K_\varepsilon^e]_{23} = -I_4\left[G^T\bar{A}^{(2)^T}\bar{C}\bar{A}^{(2)}G\right] \\ [K_\varepsilon^e]_{33} = I_6\left[G^T\bar{A}^{(2)^T}\bar{C}\bar{A}^{(2)}G\right] + I_7\left[G^T\bar{A}^{(1)^T}\bar{C}\bar{A}^{(1)}G\right] \end{cases} \tag{76}$$

$$\begin{cases} [K_\gamma^e]_{11} = B_1\left[G^T\bar{A}^{(2)^T}\bar{C}\bar{A}^{(2)}G\right] \\ [K_\gamma^e]_{12} = -B_2\left[G^T\bar{A}^{(2)^T}\bar{C}\bar{A}^{(3)}G\right] \\ [K_\gamma^e]_{13} = B_3\left[G^T\bar{A}^{(2)^T}\bar{C}\bar{A}^{(3)}G\right] \\ [K_\gamma^e]_{22} = B_1\left[G^T\bar{A}^{(2)^T}\bar{C}\bar{A}^{(2)}G\right] + B_5\left[G^T\bar{A}^{(3)^T}\bar{C}\bar{A}^{(3)}G\right] \\ [K_\gamma^e]_{23} = -B_4\left[G^T\bar{A}^{(3)^T}\bar{C}\bar{A}^{(3)}G\right] - B_7\left[G^T\bar{A}^{(2)^T}\bar{C}\bar{A}^{(2)}G\right] \\ [K_\gamma^e]_{33} = B_6\left[G^T\bar{A}^{(3)^T}\bar{C}\bar{A}^{(3)}G\right] + B_8\left[G^T\bar{A}^{(2)^T}\bar{C}\bar{A}^{(2)}G\right] \end{cases} \tag{77}$$

$$\begin{cases} [K_\eta^e]_{11} = R_1\left[G^T\bar{A}^{(2)^T}\bar{C}\bar{A}^{(2)}G\right] \\ [K_\eta^e]_{12} = -R_2\left[G^T\bar{A}^{(2)^T}\bar{C}\bar{A}^{(3)}G\right] \\ [K_\eta^e]_{13} = R_3\left[G^T\bar{A}^{(2)^T}\bar{C}\bar{A}^{(3)}G\right] - \frac{1}{2}R_8\left[G^T\bar{A}^{(2)^T}\bar{C}\bar{A}^{(1)}G\right] \\ [K_\eta^e]_{22} = \frac{2}{3}R_1\left[G^T\bar{A}^{(2)^T}\bar{C}\bar{A}^{(2)}G\right] + \frac{1}{2}R_5\left[G^T\bar{A}^{(3)^T}\bar{C}\bar{A}^{(3)}G\right] \\ [K_\eta^e]_{23} = -R_4\left[G^T\bar{A}^{(3)^T}\bar{C}\bar{A}^{(3)}G\right] + \frac{1}{2}R_9\left[G^T\bar{A}^{(3)^T}\bar{C}\bar{A}^{(1)}G\right] - \frac{2}{3}R_{11}\left[G^T\bar{A}^{(2)^T}\bar{C}\bar{A}^{(2)}G\right] \\ [K_\eta^e]_{33} = R_6\left[G^T\bar{A}^{(3)^T}\bar{C}\bar{A}^{(3)}G\right] + \frac{2}{3}R_7\left[G^T\bar{A}^{(1)^T}\bar{C}\bar{A}^{(1)}G\right] - R_{10}\left[G^T\bar{A}^{(3)^T}\bar{C}\bar{A}^{(1)}G\right] + \frac{2}{3}R_{12}\left[G^T\bar{A}^{(2)^T}\bar{C}\bar{A}^{(2)}G\right] \end{cases} \tag{78}$$

$$\begin{cases} \left[K_{\chi}^{e}\right]_{22} = D_1 \left[G^T \bar{A}^{(2)^T} \bar{C} \bar{A}^{(2)} G\right] \\ \left[K_{\chi}^{e}\right]_{23} = -\frac{1}{2} D_3 \left[G^T \bar{A}^{(2)^T} \bar{C} \bar{A}^{(2)} G\right] \\ \left[K_{\chi}^{e}\right]_{33} = \frac{1}{4} D_2 \left[G^T \bar{A}^{(1)^T} \bar{C} \bar{A}^{(1)} G\right] + \frac{1}{4} D_4 \left[G^T \bar{A}^{(2)^T} \bar{C} \bar{A}^{(2)} G\right] \end{cases} \tag{78}$$